



**HAL**  
open science

## Models for the estimation of Fe<sup>3+</sup> /Fe<sup>tot</sup> ratio in terrestrial and extraterrestrial alkali- and iron-rich silicate glasses using Raman spectroscopy

Danilo Di Genova, Kai-Uwe Hess, Oryaëlle Chevrel, Donald Dingwell

### ► To cite this version:

Danilo Di Genova, Kai-Uwe Hess, Oryaëlle Chevrel, Donald Dingwell. Models for the estimation of Fe<sup>3+</sup> /Fe<sup>tot</sup> ratio in terrestrial and extraterrestrial alkali- and iron-rich silicate glasses using Raman spectroscopy. *The American Mineralogist*, 2016, 101 (4), pp.943-952. 10.2138/am-2016-5534CCBYNCND . hal-03849788

HAL Id: hal-03849788

<https://hal.science/hal-03849788v1>

Submitted on 12 Nov 2022

**HAL** is a multi-disciplinary open access archive for the deposit and dissemination of scientific research documents, whether they are published or not. The documents may come from teaching and research institutions in France or abroad, or from public or private research centers.

L'archive ouverte pluridisciplinaire **HAL**, est destinée au dépôt et à la diffusion de documents scientifiques de niveau recherche, publiés ou non, émanant des établissements d'enseignement et de recherche français ou étrangers, des laboratoires publics ou privés.



Distributed under a Creative Commons Attribution - NonCommercial - NoDerivatives 4.0 International License

## Models for the estimation of $\text{Fe}^{3+}/\text{Fe}_{\text{tot}}$ ratio in terrestrial and extraterrestrial alkali- and iron-rich silicate glasses using Raman spectroscopy<sup>‡</sup>

DANILO DI GENOVA<sup>1,\*</sup>, KAI-UWE HESS<sup>1</sup>, MAGDALENA ORYAËLLE CHEVREL<sup>2</sup>, AND DONALD B. DINGWELL<sup>1</sup>

<sup>1</sup>Department Earth and Environmental Sciences, Ludwig-Maximilians-Universität, Theresienstrasse 41/III, 80333 München, Germany

<sup>2</sup>Departamento de Vulcanología, Instituto de Geofísica, Universidad Nacional Autónoma de México, 04510, México D.F., Mexico

### ABSTRACT

To develop Raman spectroscopy as a quantitative tool in both geosciences and planetary sciences the effect of iron oxidation state ( $\text{Fe}^{3+}/\text{Fe}_{\text{tot}}$ ) on the Raman spectra of basaltic and pantelleritic glasses has been investigated. We have used remelted pantellerite from Pantelleria Island and synthetic iron-rich basaltic glasses [from Chevrel et al. (2014)].

The Raman spectra of pantelleritic glasses reveal dramatic changes in the high wavelength region of the spectrum ( $800\text{--}1200\text{ cm}^{-1}$ ) as iron oxidation state changes. In particular the  $970\text{ cm}^{-1}$  band intensity increases with increasing oxidation state of the glass ( $\text{Fe}^{3+}/\text{Fe}_{\text{tot}}$  ratio from 0.24 to 0.83). In contrast, Raman spectra of the basaltic glasses do not show the same oxidation state sensitivity ( $\text{Fe}^{3+}/\text{Fe}_{\text{tot}}$  ratio from 0.15 to 0.79). A shift, however, of the  $950\text{ cm}^{-1}$  band to high wavenumber with decreasing iron oxidation state can be observed.

We present here two empirical parameterizations (for silica- and alkali-rich pantelleritic glasses and for iron-rich basaltic glasses) to enable estimation of the iron oxidation state of both anhydrous and hydrous silicate glasses (up to 2.4 wt%  $\text{H}_2\text{O}$ ). The validation of the models derived from these parameterizations have been obtained using the independent characterization of these melt samples plus a series of external samples via wet chemistry.

The “pantelleritic” model can be applied within  $\text{SiO}_2$ , FeO, and alkali content ranges of  $\sim 69\text{--}75$ ,  $\sim 7\text{--}9$ , and  $\sim 8\text{--}11$  wt%, respectively. The “basaltic” model is valid within  $\text{SiO}_2$ , FeO, and alkali content ranges of  $\sim 42\text{--}54$ ,  $\sim 10\text{--}22$ , and  $\sim 3\text{--}6$  wt%, respectively.

The results of this study contribute to the expansion of the compositionally dependent database previously presented by Di Genova et al. (2015) for Raman spectra of complex silicate glasses. The applications of these models range from microanalysis of silicate glasses (e.g., melt inclusions) to handheld in situ terrestrial field investigations and studies under extreme conditions such as extraterrestrial (i.e., Mars), volcanic, and submarine environments.

**Keywords:** Silicate glasses, Raman spectroscopy, iron oxidation state, redox, basalt, pantellerite, planetary science, Mars

### INTRODUCTION

The physico-chemical properties of silicate melts that govern magmatic and volcanic processes (melt generation, transport, and emplacement on the terrestrial planets) now have a long history of investigation (e.g., Richet 1984; Lange and Carmichael 1987, 1990; Persikov et al. 1990; Dingwell et al. 1996; Hess and Dingwell 1996; Papale 1999; Romano et al. 2001; Whittington et al. 2001; Dingwell 2006; Neuville 2006; Behrens and Zhang 2009; Di Genova et al. 2014a; Robert et al. 2014; Sehlke et al. 2014).

The wide range of chemical composition of magmatic and volcanic liquids means that to be useful the physico-chemical properties of these molten systems must be parameterized, directly or indirectly, in terms of chemical composition. Knowledge of the non-trivial nature of silicate melt structure and the enduring challenge of structure-property relationships for silicate melts

has fueled a generation of investigations (e.g., Mysen et al. 1982; Stolper 1982; Neuville et al. 1993; Mysen 1997; Lee and Stebbins 2003; Stebbins 2008; Xue 2009; Malfait and Sanchez-Valle 2012; Di Genova et al. 2014b).

In all of this it has long been appreciated that the oxidation state and the structural role of iron in silicate melts plays a defining role affecting the melt structure and properties (e.g., Cukierman and Uhlmann 1974; Mysen et al. 1984; Dingwell and Virgo 1987, 1988; Lange and Carmichael 1987; Dingwell et al. 1988; Dingwell 1991; Toplis et al. 1994; Toplis and Carroll 1995; Giuli et al. 2011; Chevrel et al. 2013, 2014; Knipping et al. 2015).

Iron in silicate melts appears to exhibit elements of both network former and network modifier behavior. It is typically present in a range of coordination environments from tetrahedral ( $^{\text{IV}}\text{Fe}$ ), through pentahedral ( $^{\text{V}}\text{Fe}$ ) to octahedral ( $^{\text{VI}}\text{Fe}$ ) and is always present in both reduced, ferrous ( $\text{Fe}^{2+}$ , network modifier), and oxidized, ferric ( $\text{Fe}^{3+}$ , network former) states (e.g., Mysen et al. 1984; Jackson et al. 1993; Wilke et al. 2001, 2006; Giuli et al. 2003; Magnien et al. 2008; Rossano et al. 2008).

\* E-mail: danilo.digenova@min.uni-muenchen.de

<sup>‡</sup> Open access: Article available to all readers online.

The ferric–ferrous ratio of equilibrated silicate melts depends on the temperature, redox state, and the chemical composition (including the volatile content) of the melt (Kress and Carmichael 1991; Mysen 1991; Ottonello et al. 2001; Botcharnikov et al. 2005; Moretti 2005; Giuli et al. 2012; Borisov et al. 2015; Cicconi et al. 2015). Thus a precise quantification of the ferric–ferrous ratio in silicate melts and glasses is a crucial constraint for the adequate parameterization of both the composition-dependence of physical properties (e.g., liquid viscosity and density) and the redox conditions prevailing in magmatic systems.

The most widely employed standard techniques for the direct determination of  $\text{Fe}^{3+}/\text{Fe}_{\text{tot}}$  ratio in silicate glasses are wet-chemical analyses,  $^{57}\text{Fe}$  Mössbauer spectroscopy and XANES [see Berry et al. (2003) and Mysen and Richet (2005) for reviews]. Wet chemistry is considered the most precise method, however, it is destructive and it consumes a relatively large amount of sample (in the order of 100–500 mg) for a precise  $\text{Fe}^{2+}$  concentration determination ( $\pm 0.02$ ). Standard Mössbauer spectroscopy requires powdered samples (in the order of 50–100 mg) for an accurate estimation of  $\text{Fe}^{3+}/\text{Fe}_{\text{tot}}$  ( $\pm 0.02$ ) and, in addition, it is relatively limited in spatial resolution (McCammon et al. 1991; Berry et al. 2003 and references therein). Fe *K*-edge XANES spectroscopy requires a smaller amount of material and it has been employed also on small amount of glass and it is characterized by a high spatial resolution (micrometers). Nevertheless, despite the wide applicability of this technique, three main points must be considered: (1) the fitting procedure of the Fe pre-edge peak is not easy and the  $\text{Fe}^{3+}/\text{Fe}_{\text{tot}}$  estimation is associated with a high error ( $\pm 0.05$ ) respect to wet chemistry and Mössbauer; (2) for low amount of total iron, photoreduction by synchrotron beam has been reported (Campeny et al. 2015); and (3) XANES spectroscopy is not easily accessible as it requires beam time at a synchrotron radiation facility.

Raman spectroscopy is a technique commonly used for studying the structure of silicate glasses and melts (Neuvville et al. 2014 for a review). It offers the advantages that (1) little or no sample preparation is required, (2) the technique is non-destructive, and (3) can be used to perform in situ and remotely controlled analysis under extreme conditions like, for example, submarine environment or on planetary surfaces [see Di Genova et al. (2015) and references therein for a review].

Only one study (Di Muro et al. 2009) has raised the possibility of retrieving information on the  $\text{Fe}^{3+}/\text{Fe}_{\text{tot}}$  ratio of natural silicate glasses (pantelleritic and basaltic compositions) by Raman spectroscopy.

Results from Di Muro et al. (2009) show a dependence of Raman spectra for some remelted silicate glasses on iron oxidation state. They demonstrate the existence of a relationship between the measured  $\text{Fe}^{3+}/\text{Fe}_{\text{tot}}$  ratio (by wet chemistry and XANES spectroscopy) and the Raman parameters derived by spectra deconvolution (e.g., area%, band position, and bands intensity ratio). In particular, because of the significant sensitivity of Raman spectra of pantelleritic samples with the variation in  $\text{Fe}^{3+}/\text{Fe}_{\text{tot}}$  ratio, the authors concluded that peralkaline glasses represent an ideal system to define a Raman model to estimate the iron oxidation state of samples. On the other hand, their results on basaltic samples demonstrated the decreasing sensitivity of the glass structure, and consequently of Raman spectra, with

changing redox conditions of the system.

Unfortunately, as those authors reported, this approach depends strongly on both the spectra fitting procedure (i.e., spectrum deconvolution) and the chemical composition of samples [see Rossano and Mysen (2012) and Neuvville et al. (2014) for reviews].

Recently, Di Genova et al. (2015) have demonstrated that the chemical composition of natural silicate glasses could be approximated using Raman spectroscopy *without* the use of a spectra deconvolution procedure.

In this work, we combine wet-chemical analysis and Raman spectroscopy to track the evolution of the Raman spectra as a function of  $\text{Fe}^{3+}/\text{Fe}_{\text{tot}}$  ratio of remelted and synthetic silicate glasses. The evolution of the acquired Raman spectra has been parameterized using the empirical criterion presented in Di Genova et al. (2015), which is based on an ideal mixing equation, to provide two Raman spectroscopy models for determining the  $\text{Fe}^{3+}/\text{Fe}_{\text{tot}}$  ratio of silica-alkali-rich and iron-rich basalt silicate glasses (anhydrous and mildly hydrous) in terrestrial and extra-terrestrial environments.

## EXPERIMENTAL METHODS

### Starting material

In this study, the starting material consist of (1) anhydrous, crystals, and bubble-free silica- and alkali-rich glasses of pantelleritic composition (i.e., peralkaline rhyolite, Fsp sample series) with different  $\text{Fe}^{3+}/\text{Fe}_{\text{tot}}$  ratio that were prepared by melting a natural sample from Cala di Tramontana (Pantelleria Island), at 1500 °C and homogenized by continuous stirring in a concentric cylinder apparatus at 1 atm until the melt was free of bubbles and crystals; (2) anhydrous, crystals, and bubble-free iron-rich (up to ~20 wt%  $\text{FeO}_{\text{tot}}$ ) basaltic glasses (AdMB and LDM series) representative of the known diversity of martian basalts with different  $\text{Fe}^{3+}/\text{Fe}_{\text{tot}}$  ratios from Chevrel et al. (2014). The AdMB chemical composition corresponds to the chemical analyses of the Adirondack class rock (Gusev plains, Mars) as given by Ming et al. (2008). The LDM chemical composition is based on equilibrium melting calculations of a primitive mantle composition [see Baratoux et al. (2011) and Chevrel et al. (2014) for details].

Both sets of samples were synthesized at different oxygen fugacity,  $f_{\text{O}_2}$ , in a gas-mixing furnace to obtained glasses with different  $\text{Fe}^{3+}/\text{Fe}_{\text{tot}}$  ratio (as described in Chevrel et al. 2014). The furnace is equipped with a gas tight alumina muffle tube and CO-CO<sub>2</sub> gas mixing line. The  $f_{\text{O}_2}$  was controlled by CO-CO<sub>2</sub> gas mixtures and monitored by an yttrium-stabilized, zirconia-based oxygen electrode calibrated against air and pure CO<sub>2</sub>. At least 24 h was required to permit melt equilibration for each oxidation step. Sampling was performed after each equilibration by a “dip quench” technique that consisted of inserting an alumina-oxide rod into the melt, which was then withdrawn and plunged into distilled water to ensure a rapid quench. All glasses were verified to be free from crystals by optical and electron microscopy.

### Iron oxidation state

The iron oxidation state of the investigated samples was determined by redox titration using potassium dichromate ( $\text{K}_2\text{Cr}_2\text{O}_7$ ): a wet-chemistry method based on a simple potentiometric titration (Giuli et al. 2011). The standard materials used for the evaluation of the standard deviation of the measurements were a standard rock basalt (BHVO-1, USGS standard, Lit. 8.58 wt% FeO) and a synthetic standard containing 18.8 wt% of FeO. The standard deviation of the measurements was determined to be  $\pm 1.5\%$ . Each measurement was performed with approximately 25 mg of sample.

### Chemical analysis

The concentrations of major elements were measured with a Cameca SX100 electron microprobe analyzer (EMPA) of the Department of Earth and Environmental Sciences at the University of Munich. The chemical analyses were carried out at 15 kV acceleration voltage and 5 nA beam current. A defocused 10  $\mu\text{m}$  beam was used for all elements to minimize alkali loss. Synthetic wollastonite (Ca, Si), periclase (Mg), hematite (Fe), corundum (Al), natural orthoclase (K), and albite (Na) were used as standards, and matrix correction was performed by

PAP procedure (Pouchou and Pichoir 1991). The precision was better than 2.5% for all analyzed elements. To evaluate the chemical homogeneity of glasses 25 chemical analyses were performed for each sample. As reported in Chevrel et al. (2014), a liquid immiscibility in the iron-rich basalt glasses can be observed. This aspect does not represent a limitation in our study, as the Raman spot size is much smaller than the characteristic dimension of the liquid-liquid immiscibility (from tens to hundreds of micrometers).

### Raman spectroscopy

Raman spectra were obtained using a micro-Raman spectrometer (HORIBA; XploRa-Raman-System) equipped with three lasers (red, green, and NIR). A green argon ion laser (532 nm), which provided a power at the sample surface of ~2.5 mW, was focused through the 100× objective to a ~1 μm spot. The Raman system was set with a laser attenuation of 25% in respect to the total laser power, 1200T grating, exposure time 30 s (3 times), and confocal hole of 300 μm and slit of 200 μm. Backscattered Raman radiation was collected over a range from 150 to 1400 cm<sup>-1</sup> and elastically scattered photons were suppressed via a sharp edge filter. The instrument was calibrated using a silicon standard.

All the acquired spectra have been corrected for the wavelength of excitation source and temperature dependence of the Raman intensity according to Shuker and Cammon (1970) and Long (1977) approaches. Finally, a background subtraction technique has been applied to all the spectra according to the strategy reported in Di Genova et al. (2015) where two zones devoid of peaks were chosen to constrain the cubic baseline (from 50 to ~250 and ~1250 to 1500 cm<sup>-1</sup>).

## RESULTS

### Chemical composition and iron oxidation state

Measured chemical compositions and Fe<sup>3+</sup>/Fe<sub>tot</sub> ratio of pantelleritic (this study) and basaltic (Chevrel et al. 2014) glasses are reported in Table 1.

Additionally, in Figure 1 we report in a TAS diagram the chemical compositions of both the pantelleritic and basaltic end-members (Fsp\_1, Fsp\_9 and AdMB-S2, LDM-S5, respectively).

Pantelleritic samples include nine different glasses with different Fe<sup>3+</sup>/Fe<sub>tot</sub> ratios ranging between 0.24 and 0.83, and having an aegaitic index [(Na<sub>2</sub>O+K<sub>2</sub>O)/Al<sub>2</sub>O<sub>3</sub> mol%] of around 1.3. Main oxides range between ~72–75 wt% SiO<sub>2</sub>, ~7–9 wt% FeO<sub>tot</sub>, ~9 wt% Al<sub>2</sub>O<sub>3</sub>, and alkali (Na<sub>2</sub>O+K<sub>2</sub>O) between ~8 and 11 wt%.

Basaltic samples are highly enriched in iron [FeO<sub>tot</sub> ranging from ~18 to ~20 wt%] as analyzed on Mars [see Chevrel et al. (2014)] and include four glasses having different Fe<sup>3+</sup>/Fe<sub>tot</sub> ratio ranging between 0.15 and 0.79. Specifically, we used three AdMB samples (AdMB-S2, S5, and S6) and one sample (LDM-S5) belonging to the LDM series that represents the sample with the lowest Fe<sup>3+</sup>/Fe<sub>tot</sub> ratio among the analyzed samples in Chevrel et al. (2014). SiO<sub>2</sub> varies between ~45–48 wt%, Al<sub>2</sub>O<sub>3</sub> is ~11 wt%,

and alkali and alkaline earth (MgO+CaO) range between ~3–4 and ~18–20 wt%, respectively.

### Raman spectra: Effect of the chemical composition

Figures 2 and 3 show the Raman spectra acquired, corrected for the wavelength of the excitation source and temperature. The raw spectra are reported in Figures 2a and 3a, while Figures 2b and 3b show the normalized spectra (to 100 arbitrary units) vertically superimposed as a function of the Fe<sup>3+</sup>/Fe<sub>tot</sub> ratio.

The collected Raman spectra show three main bands: the low-wavenumber region (LW ~250–650 cm<sup>-1</sup>), the mid-wavenumber region (MW ~650–850 cm<sup>-1</sup>) and in the high-wavenumber region (HW ~850–1250 cm<sup>-1</sup>).

The LW region is usually assigned to vibrations of bridging O atoms (BO) with three-, four-, five-, six-, or higher-membered rings of tetrahedra present in silicate networks (e.g., Bell et al. 1968; Mysen et al. 1980; McMillan and Piriou 1982; Seifert et al. 1982; Neuville and Mysen 1996; Pasquarello et al. 1998; Mysen 2003; Umari et al. 2003; Neuville et al. 2014). The HW region yields information about the vibration of T–O<sup>-</sup> bonds [where T refers to fourfold-coordinated cations (Si<sup>4+</sup>, Al<sup>4+</sup>, Fe<sup>3+</sup>) and O<sup>-</sup> non-bridging oxygen, NBO] and the structural effect of the network-modifying or charge balancing cations (e.g., Bell and Dean 1972; Furukawa et al. 1981; McMillan 1984; Mysen 2003; Mysen and Toplis 2007; Neuville et al. 2014). For a detailed discussion of structural interpretation of Raman spectra we refer to Rossano and Mysen (2012) and Neuville et al. (2014).

Overall, the LW region of pantelleritic samples (Fig. 2a) shows a well-defined band between 250 and 650 cm<sup>-1</sup> with a peak located around 470 cm<sup>-1</sup> and a shoulder at 590 cm<sup>-1</sup>. In contrast, the LW region of basaltic spectra (Fig. 3a) shows an asymmetric band centered around 550 cm<sup>-1</sup> and overlapping with the MW region.

In the MW region, a symmetric band occurs between 670 and 850 cm<sup>-1</sup> in the spectra of all investigated samples and shows the highest intensity in the basaltic spectra.

Concerning the HW region, the pantelleritic spectra display a complex behavior of the band located between 850 and 1250 cm<sup>-1</sup>. The most oxidized sample (Fsp\_1) shows a peak located at 970 cm<sup>-1</sup> and two shoulders at 1040 and 1150 cm<sup>-1</sup> while the most reduced sample (Fsp\_9) clearly shows a peak at around 1040 cm<sup>-1</sup> with two shoulders at 970 and 1150 cm<sup>-1</sup>.

**TABLE 1.** Chemical composition and iron oxidation state of analyzed glasses

Sample	SiO <sub>2</sub>	TiO <sub>2</sub>	Al <sub>2</sub> O <sub>3</sub>	FeO	MnO	MgO	CaO	Na <sub>2</sub> O	K <sub>2</sub> O	P <sub>2</sub> O <sub>5</sub>	Tot.	Fe <sup>3+</sup> /Fe <sub>tot</sub> <sup>b</sup>	Fe <sup>3+</sup> /Fe <sub>tot</sub> <sup>calc</sup> <sup>c</sup>
Fsp_1	72.53	0.44	8.70	9.02	0.34	0.17	0.45	4.59	4.09	0.00	100.33	0.83	0.86
Fsp_2	71.89	0.43	8.78	8.78	0.35	0.16	0.43	4.37	4.01	0.00	99.20	0.74	0.76
Fsp_3	72.94	0.42	8.92	8.55	0.37	0.17	0.44	4.46	4.10	0.00	100.37	0.58	0.58
Fsp_4	71.93	0.43	8.97	8.93	0.37	0.17	0.46	4.72	4.18	0.00	100.16	0.62	0.56
Fsp_5	73.75	0.41	9.06	7.73	0.30	0.15	0.37	4.08	3.94	0.00	99.79	0.69	0.69
Fsp_6	73.11	0.43	8.97	8.34	0.37	0.17	0.47	4.55	4.18	0.00	100.59	0.40	0.43
Fsp_7	73.44	0.43	9.05	7.71	0.35	0.17	0.40	4.08	3.99	0.00	99.62	0.35	0.33
Fsp_8	74.62	0.45	9.05	7.17	0.38	0.18	0.45	4.06	4.05	0.00	100.41	0.26	0.27
Fsp_9	74.24	0.44	9.01	7.04	0.36	0.17	0.47	4.19	4.14	0.00	100.06	0.24	0.24
AdMB-S2 <sup>a</sup>	46.77	0.61	10.93	19.65	0.44	9.23	8.73	2.88	0.18	0.57	100.00	0.79	0.79
AdMB-S5 <sup>a</sup>	47.46	0.58	10.98	19.41	0.44	8.97	8.59	2.84	0.18	0.57	100.00	0.52	0.49
AdMB-S6 <sup>a</sup>	47.62	0.64	11.13	18.95	0.43	9.13	8.53	2.84	0.17	0.57	100.00	0.37	0.36
LDM-S5 <sup>a</sup>	45.17	0.71	10.47	18.09	0.14	11.28	8.96	3.91	0.29	0.98	100.00	0.15	0.15

<sup>a</sup> From Chevrel et al. (2014) (normalized to 100 wt%).

<sup>b</sup> Obtained by wet chemistry.

<sup>c</sup> Calculated Fe<sup>3+</sup>/Fe<sub>tot</sub> ratio using Equation 2.

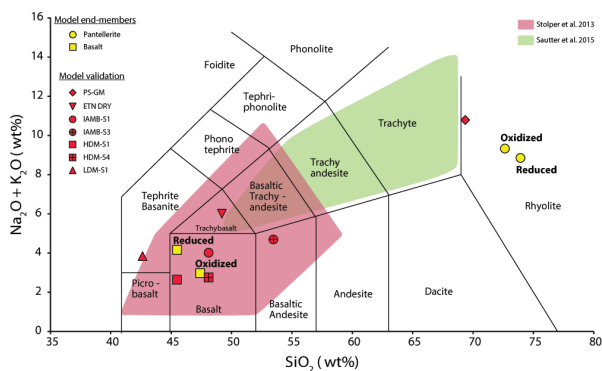


**FIGURE 1.** Total alkali vs.  $\text{SiO}_2$  contents in wt% (TAS) diagram showing the chemical composition of glasses used in this study. Yellow symbols represent the input chemical composition (oxidized and reduced) used to develop the Raman models (Eq. 1). Red symbols represent the samples used for the model validation. Red and green areas show the interval of chemical compositions measured on Mars and from martian meteorites according to Stolper et al. (2013) and Sautter et al. (2015).

In contrast, for the basaltic samples, the band occurs between 800 and 1200  $\text{cm}^{-1}$  with a peak between 950 and 966  $\text{cm}^{-1}$  a shoulder located at  $\sim 1040 \text{ cm}^{-1}$  and show less variation with oxidation as detailed below.

### Raman spectra: Effect of $\text{Fe}^{3+}/\text{Fe}_{\text{tot}}$ ratio

To explore the evolution of Raman spectra with the oxidation state, and provide Raman models to estimate the  $\text{Fe}^{3+}/\text{Fe}_{\text{tot}}$  ratio, we vertically superimposed the normalized Raman spectra as a function of  $\text{Fe}^{3+}/\text{Fe}_{\text{tot}}$  ratio (Figs. 2b and 3b).

### Pantelleritic glasses

Figure 2b shows the normalized Raman spectra as a function of the  $\text{Fe}^{3+}/\text{Fe}_{\text{tot}}$  ratio. In the LW region, both the intensities of the peak located at  $\sim 470 \text{ cm}^{-1}$  and the shoulder located at  $\sim 590 \text{ cm}^{-1}$  decrease with increasing the  $\text{Fe}^{3+}/\text{Fe}_{\text{tot}}$  ratio. Similarly in the MW region the peak located at  $\sim 800 \text{ cm}^{-1}$  decreases in intensity with increasing the  $\text{Fe}^{3+}/\text{Fe}_{\text{tot}}$ .

The HW region exhibits a remarkable variation of the Raman spectrum with  $\text{Fe}^{3+}/\text{Fe}_{\text{tot}}$  ratio. Indeed, with increasing  $\text{Fe}^{3+}/\text{Fe}_{\text{tot}}$  ratio, the wavelength position of the band centroid shifts toward low wavenumbers: from 1040  $\text{cm}^{-1}$  (Fsp\_9,  $\text{Fe}^{3+}/\text{Fe}_{\text{tot}} = 0.24$ ) down to 970  $\text{cm}^{-1}$  (Fsp\_1,  $\text{Fe}^{3+}/\text{Fe}_{\text{tot}} = 0.83$ ) and the shoulder located at 970  $\text{cm}^{-1}$  dramatically decreases in intensity. Concurrently, the shoulder located at 1150  $\text{cm}^{-1}$  decreases in intensity with increasing  $\text{Fe}^{3+}/\text{Fe}_{\text{tot}}$  ratio. The most oxidized sample (Fsp\_1) therefore shows a peak located at 970  $\text{cm}^{-1}$  and two shoulders at 1040 and 1150  $\text{cm}^{-1}$ , while the most reduced sample (Fsp\_9) clearly shows a peak at around 1040  $\text{cm}^{-1}$  with two shoulders at 970 and 1150  $\text{cm}^{-1}$ .

### Basaltic glasses

Although the Raman spectra of the basaltic samples exhibit a weaker variation with  $\text{Fe}^{3+}/\text{Fe}_{\text{tot}}$  ratio than the pantelleritic samples, some variations can be pointed out (Fig. 3b).

The intensity in LW and MW region increases with increasing  $\text{Fe}^{3+}/\text{Fe}_{\text{tot}}$  ratio. In the HW region, the main peak position shifts toward low wavenumber with increasing the  $\text{Fe}^{3+}/\text{Fe}_{\text{tot}}$  ratio.

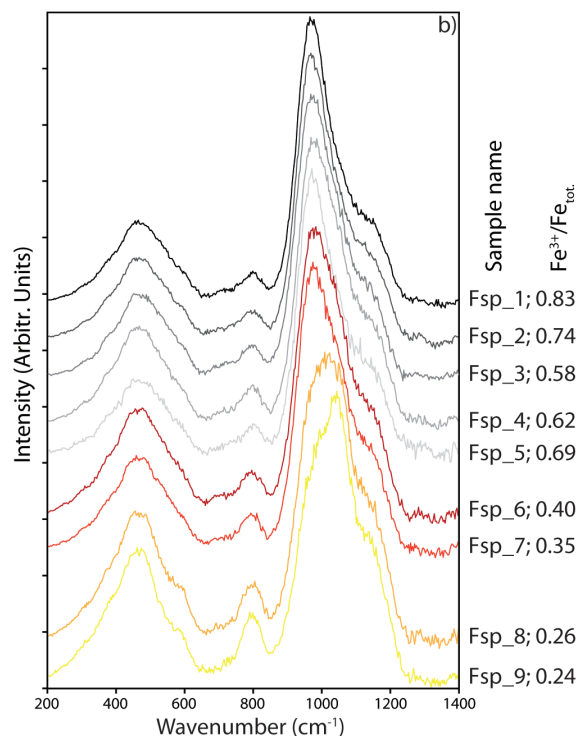
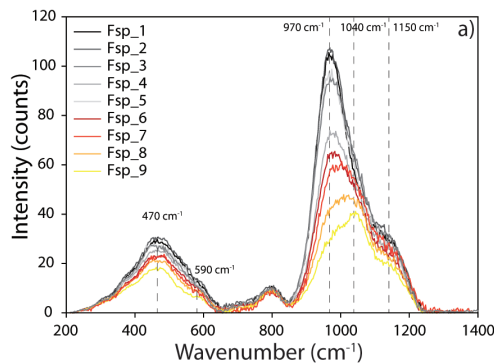


**FIGURE 2.** (a) Raw Raman spectra after a cubic baseline correction of silica-alkali-rich samples (Fsp, pantellerite). Vertical dashed lines represent the main peaks and shoulders of the spectra. (b) Raman spectra corrected according to Equation 2 and normalized to the most intense peak.

Indeed, the reduced end-member (LDM-S5,  $\text{Fe}^{3+}/\text{Fe}_{\text{tot}} = 0.15$ ) exhibits the peak at 966  $\text{cm}^{-1}$  while the oxidized end-member (AdMB-S2,  $\text{Fe}^{3+}/\text{Fe}_{\text{tot}} = 0.79$ ) has the peak at 950  $\text{cm}^{-1}$ . The samples characterized by an intermediate iron oxidation state show intermediate main peak position at 963 and 961  $\text{cm}^{-1}$  for AdMB-S6,  $\text{Fe}^{3+}/\text{Fe}_{\text{tot}} = 0.37$  and for AdMB-S5,  $\text{Fe}^{3+}/\text{Fe}_{\text{tot}} = 0.52$ , respectively. Additionally, a decrease of the shoulder intensity ( $\sim 1040 \text{ cm}^{-1}$ ) occurs with increasing  $\text{Fe}^{3+}/\text{Fe}_{\text{tot}}$  ratio.

## DISCUSSION

The results presented here generally agree with those of Di Muro et al. (2009). Pantelleritic Raman spectra in this study show

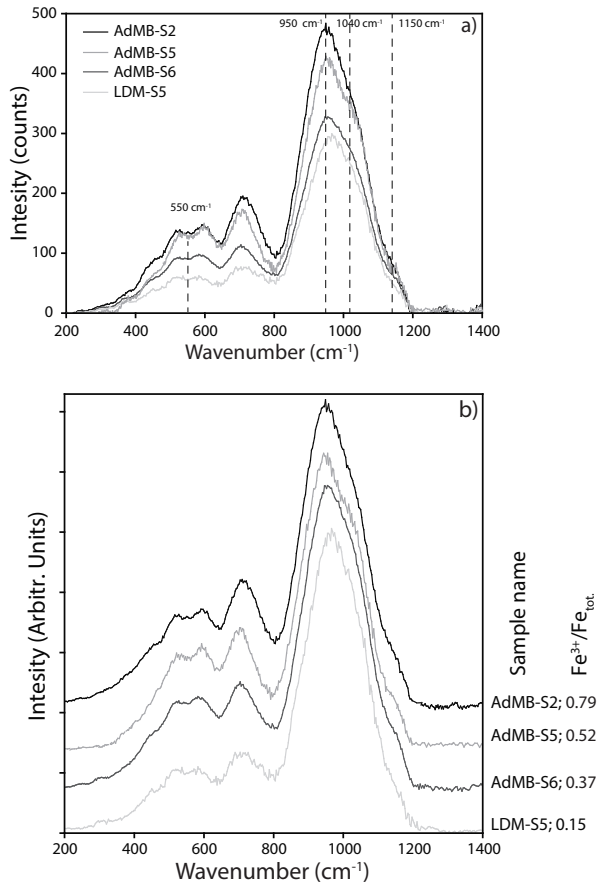


**FIGURE 3.** (a) Raw Raman spectra after a cubic baseline correction of iron-rich samples (AdMB and LDM, martian basalts). Vertical dashed lines represent the main peaks and shoulders of the spectra. (b) Raman spectra corrected according to Equation 2 and normalized to the most intense peak.

a dramatic variation with changing the  $\text{Fe}^{3+}/\text{Fe}_{\text{tot}}$  ratio while a weak sensitivity of Raman spectra is observed for the basaltic glasses with changing iron oxidation state.

Our approach differs however in one important aspect from that employed by Di Muro et al. (2009). As noted above, we avoid the highly disputed use of deconvolution bands (Rossano and Mysen 2012; Neuville et al. 2014). Instead we adopt the criterion reported in Di Genova et al. (2015) based on an empirical approach to parameterize Raman spectra using an ideal mixing equation (reported below). This approach provides a robust strategy to determine the iron oxidation state of glasses, independent of the chemical composition of the samples investigated. Furthermore, using this approach, together with iron-rich basaltic glasses (suitable for planetary science studies), the limitation due to the low sensitivity of Raman spectra to different iron oxidation states (for depolymerized compositions like basalt) is overcome.

#### Parameterization of the evolution of Raman spectra

To evaluate Raman spectroscopy as a tool to estimate the iron oxidation state of glasses we combine the acquired Raman spectra (Figs. 2b and 3b) with measured  $\text{Fe}^{3+}/\text{Fe}_{\text{tot}}$  ratios (Table 1) using

the model presented in Di Genova et al. (2015).

We used an empirical formula (Eq. 1) previously reported in Di Genova et al. (2015) to parameterize the Raman spectra as a function of a fit parameter ( $R_p$ ). Specifically we assume that an acquired Raman spectrum can be approximate combining two end-members Raman spectra with the Raman parameter  $R_p$ :

$$Y = E_{\text{ox}} \cdot R_p + E_{\text{RED}}(1 - R_p) \quad (1)$$

where  $Y$  represents the acquired Raman spectrum of the investigated sample, and  $E_{\text{ox}}$  and  $E_{\text{RED}}$  represent the Raman spectra end-members, namely the most oxidized (Fsp\_1 and AdMB-S2) and the most reduced (Fsp\_9 and LDM-S5) samples for the pantelleritic and basaltic glasses, respectively. The  $R_p$  fit parameter was calculated for each acquired Raman spectra using Equation 1, and has been reported and plotted in Table 2 and Figure 4 together with the measured  $\text{Fe}^{3+}/\text{Fe}_{\text{tot}}$  ratios.

It must be noted that the  $R_p$  parameter is equal to 1 when only the most oxidized end-members are considered (Fsp\_1 and AdMB-S2) and, on the other hand, is equal to 0 when only the most reduced end-members are considered (Fsp\_9 and LDM-S5).

The two different compositions clearly exhibit trends with respect to the calculated Raman parameter vs.  $\text{Fe}^{3+}/\text{Fe}_{\text{tot}}$  ratio. For this reason, these trends were parameterized as a function of the Raman parameter ( $R_p$ ) to calculate the  $\text{Fe}^{3+}/\text{Fe}_{\text{tot}}$  ratio of glasses.

#### Raman models to calculate the $\text{Fe}^{3+}/\text{Fe}_{\text{tot}}$ ratio of silicate glasses

We parameterized the  $\text{Fe}^{3+}/\text{Fe}_{\text{tot}}$  ratio as a function of  $R_p$  parameter using the following equation:

$$\frac{\text{Fe}^{3+}}{\text{Fe}_{\text{tot}}} = \sqrt{\frac{(a + cR_p)}{(1 + bR_p)}} \quad (2)$$

where  $a$ ,  $b$ , and  $c$  are the best-fit parameters. Finally, using the Equation 2 with the fit parameters reported in Table 3 (for pantelleritic and basaltic glasses) and the calculated  $R_p$  parameters using Equation 1 (Table 2), we can accurately estimate the  $\text{Fe}^{3+}/\text{Fe}_{\text{tot}}$  ratio of our samples simply using the acquired Raman spectra. In Table 1 we report the calculated  $\text{Fe}^{3+}/\text{Fe}_{\text{tot}}$  ratios, while in Figure 5 we show the comparison between measured and calculated iron oxidation state of our samples.

#### Validation of the models

To validate our approach, we have investigated 11 other samples. For this purpose, we have used six natural glasses, anhydrous and water-bearing, with different  $\text{Fe}^{3+}/\text{Fe}_{\text{tot}}$  ratios: three pantelleritic glasses from Pantelleria Island (PS series in Di Genova et al. 2013, 2014a) and three basaltic glasses from Etna (ETN series in Di Genova et al. 2014a). In addition, we have used five iron-rich basaltic glasses with different  $\text{Fe}^{3+}/\text{Fe}_{\text{tot}}$  ratios (analogs for extra-terrestrial basalt, from the IAMB, LDM, HDM series in Chevrel et al. 2014). Chemical compositions are reported in Table 4 together with the measured iron oxidation state and water content and, in addition, are shown in a TAS diagram (Fig. 1).

The acquired Raman spectra are reported in Figure 6. In Table

**TABLE 2.** Calculated  $R_p$  parameter using Equation 1

Sample	$\text{Fe}^{3+}/\text{Fe}_{\text{tot}}$	$R_p$
Fsp_1	0.83	1.000
Fsp_2	0.74	0.947 (0.004)
Fsp_3	0.58	0.793 (0.008)
Fsp_4	0.62	0.770 (0.009)
Fsp_5	0.69	0.903 (0.007)
Fsp_6	0.40	0.564 (0.011)
Fsp_7	0.35	0.314 (0.014)
Fsp_8	0.26	0.104 (0.013)
Fsp_9	0.24	0.000
AdMB-S2	0.79	1.000
AdMB-S6	0.37	0.684 (0.017)
HDM-S1	0.77	1.000 (0.011)
LDM-S5	0.15	0.000

4 we report, for each sample, the chemical compositions, the measured iron oxidation state, and water content together with the calculated  $R_p$  parameters using Equation 1 and the estimated  $\text{Fe}^{3+}/\text{Fe}_{\text{tot}}$  ratio using our models (Eq. 2 and fit parameters in Table 3). A comparison between the estimated and the measured  $\text{Fe}^{3+}/\text{Fe}_{\text{tot}}$  ratio is reported in Figure 7. As can be seen in the figure the calculated  $\text{Fe}^{3+}/\text{Fe}_{\text{tot}}$  ratio of the investigated sample are well

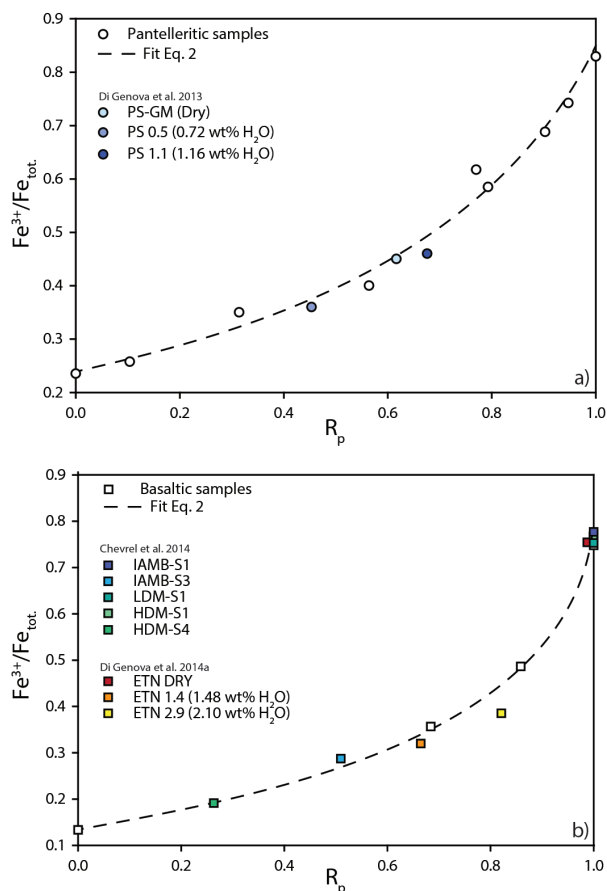


**FIGURE 4.** Measured iron oxidation states as a function of the calculated Raman parameter ( $R_p$ ) using Equation 1 for (a) pantelleritic and (b) basaltic samples. Lines represent the fits obtained using Equation 2 and fit parameters reported in Table 3. White symbols represent the samples used for model parameterization and colored symbols represent external samples used for model validation.

**TABLE 3.** Fit parameters used to parameterize the  $\text{Fe}^{3+}/\text{Fe}_{\text{tot}}$  ratio (Eq. 2) as a function of the  $R_p$  parameter (Eq. 1)

	$a$	$b$	$c$	$R^2$
Pantellerite	0.0571 (0.0061)	-0.8189 (0.0570)	0.0760 (0.0288)	0.984
Basalt	0.0223 (0.0039)	-0.9007 (0.0300)	0.0391 (0.0131)	0.996

in accordance with the measured values.

Upon inspection of Table 4 it is possible to assess quantitatively the validity of our models to determine the iron oxidation state of silicate glasses. In particular, the anhydrous pantelleritic glass (PS-GM) exhibits a measured  $\text{Fe}^{3+}/\text{Fe}_{\text{tot}}$  ratio of 0.36, while the calculated ratio using our model is 0.38. Concerning the anhydrous analogs extra-terrestrial basalt (IAMB, LDM, HDM series), the estimated  $\text{Fe}^{3+}/\text{Fe}_{\text{tot}}$  ratio is 0.79, 0.28, 0.79, 0.21, and 0.79 for IAMB-S1 and -S3, HDM-S1 and -S4 and LDM-S1 samples, respectively, while the measured  $\text{Fe}^{3+}/\text{Fe}_{\text{tot}}$  ratios are 0.79, 0.31, 0.77, 0.20, and 0.77.

Although our models have been developed using volatile-free samples, we used water-bearing samples (PS 0.5, PS 1.1, ETN 1.4, and ETN 2.9) to verify the accuracy of our models in predicting the iron oxidation state. It must be noted that a water-bearing glass represent an extreme scenario for testing our model as the water has the biggest effects, among all the magmatic volatiles (e.g.,  $\text{H}_2\text{O}$ ,  $\text{CO}_2$ , F, Cl) in affecting the silicate structure (Di Genova et al. 2014a and references therein) and, consequently, the Raman spectra.

In particular, for pantelleritic water-bearing glasses, our model accurately predicts the measured  $\text{Fe}^{3+}/\text{Fe}_{\text{tot}}$  ratio. Indeed, sample PS 0.5, characterized by a water content of 0.72 wt%, exhibits a  $\text{Fe}^{3+}/\text{Fe}_{\text{tot}}$  ratio of 0.46, while the calculated  $\text{Fe}^{3+}/\text{Fe}_{\text{tot}}$  ratio is 0.49. At the same time, sample PS 1.1 that is characterized by a higher water content (1.16 wt%) with respect to PS 0.5, exhibits a  $\text{Fe}^{3+}/\text{Fe}_{\text{tot}}$  ratio of 0.45 while the calculated ratio is 0.47. We did not validate our model to predict the oxidation state of a pantelleritic samples with a high water content (2.10 wt%  $\text{H}_2\text{O}$ ). The difficulty to estimate the  $\text{Fe}^{3+}/\text{Fe}_{\text{tot}}$  ratio of such water-rich samples is probably due the large effect of this amount of water on the Raman spectrum.

Regarding the basaltic samples, the model can accurately predict the iron oxidation state (measured  $\text{Fe}^{3+}/\text{Fe}_{\text{tot}} = 0.32$ , calculated = 0.35) for sample with minor water content (ETN 1.4,  $\text{H}_2\text{O}$  1.48 wt%), however the model shows large errors when the sample with the highest water content is considered (ETN 2.9,  $\text{H}_2\text{O}$  2.40 wt%). The measured  $\text{Fe}^{3+}/\text{Fe}_{\text{tot}}$  ratio is 0.39, while the calculated ratio is 0.48.

For these reasons we stress that care must be taken in applying our models to water-rich samples (i.e., higher than 2.10 and 2.40 wt% for pantelleritic and basaltic samples), because the strong effects of water on the glass structure and, therefore, on the Raman spectra.

### How to use the models

The Excel version of our models is provided as Supplemental Material<sup>1</sup>. First of all, a Raman spectrum has to be acquired, and we suggest setting the Raman system on how it is reported in

<sup>1</sup> Deposit item AM-16-45534, Supplemental Material, Excel calculator for the estimation of iron oxidation state in silicate glasses. Deposit items are free to all readers and found on the MSA web site, via the specific issue's Table of Contents (go to <http://www.minsocam.org/MSA/AmMin/TOC/>).

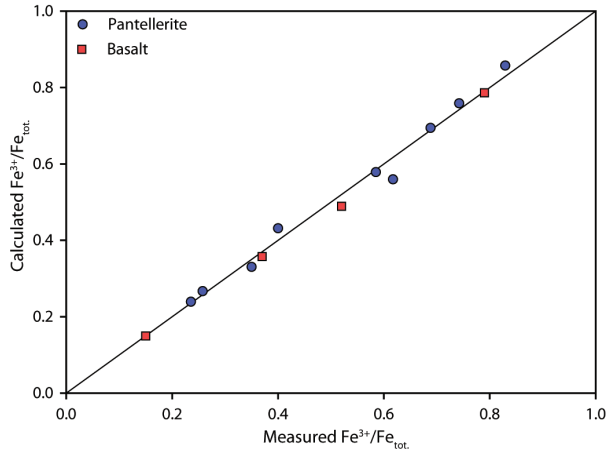


**FIGURE 5.** Comparison between measured Fe<sup>3+</sup>/Fe<sub>tot</sub> ratio using wet chemistry and calculated Fe<sup>3+</sup>/Fe<sub>tot</sub> using our proposed Raman models (Eq. 2 and fitting parameters of Tables 2 and 3) for the samples used in this study. Fe<sup>3+</sup>/Fe<sub>tot</sub> ratios are reported in Table 1.

the Raman Spectroscopy paragraph. Subsequently, the following correction has to be applied to the acquired Raman spectrum [see Shuker and Cammon (1970) and Long (1977) for the theoretical background]:

$$I = I_{\text{obs}} \cdot \left\{ v_0^3 \cdot v \frac{[1 - \exp(-hc\nu/kT)]}{(v_0 - \nu)^4} \right\} \quad (3)$$

where  $I_{\text{obs}}$  is the acquired Raman spectra;  $h$  is the Planck constant,  $h = 6.62607 \times 10^{-34}$  J s;  $k$  is the Boltzmann constant;  $k = 1.38065 \times 10^{-23}$  J K<sup>-1</sup>;  $c$  is the speed of light,  $c = 2.9979 \times 10^{10}$  cm s<sup>-1</sup>;  $T$  is the absolute temperature,  $v_0$  is the wavenumber of the incident laser light (10<sup>7</sup>/532 for the green laser), and  $\nu$  is the measured wavenumber in cm<sup>-1</sup>.

After applying the correction, the background subtraction has to be applied to the acquired spectrum (see the Raman Spectroscopy paragraph) together with an intensity normalization to 100 (arbitrary units).

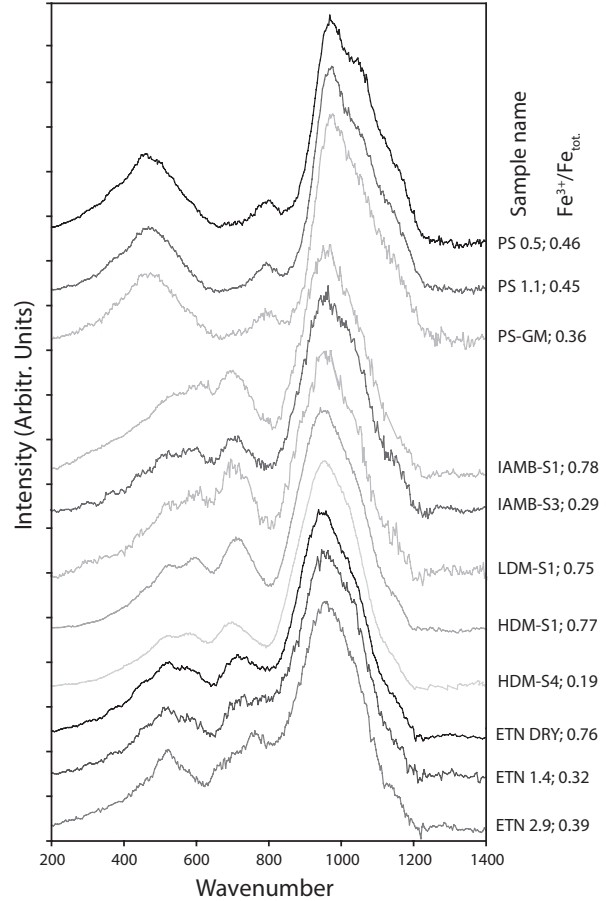


**FIGURE 6.** Long-corrected and normalized Raman spectra of samples used to validate our Raman models. PS and ETN samples are from Di Genova et al. (2013, 2014a), while the remaining samples are from Chevrel et al. (2014).

Finally, before using the Excel file<sup>1</sup>, it is important to verify that the three different Raman spectra (two end-members spectra and the sample spectrum) have to be necessarily characterized by the same  $X$  values (cm<sup>-1</sup>).

**TABLE 4.** Chemical composition and iron oxidation state of the analyzed external samples used to test the proposed Raman model; the calculated iron oxidation state using the Equation 2 and the calculated Raman parameter ( $R_p$ ) are also reported

Sample	SiO <sub>2</sub>	TiO <sub>2</sub>	Al <sub>2</sub> O <sub>3</sub>	FeO	MnO	MgO	CaO	Na <sub>2</sub> O	K <sub>2</sub> O	P <sub>2</sub> O <sub>5</sub>	Cr <sub>2</sub> O <sub>3</sub>	H <sub>2</sub> O	Total	Fe <sup>3+</sup> /Fe <sub>tot</sub>	$R_p^b$	Fe <sup>3+</sup> /Fe <sub>tot</sub> <sup>calc c</sup>
PS-GM <sup>a</sup>	69.21	0.50	9.18	8.63	0.32	0.08	0.60	6.52	4.35	0.04	–	0.00	99.43	0.36	0.640 (0.012)	0.38
PS0.5 <sup>d</sup>	70.02	0.49	9.18	8.30	0.39	0.08	0.59	5.94	3.96	0.04	0.01	0.72	99.72	0.46	0.454 (0.018)	0.49
PS1.1 <sup>d</sup>	69.78	0.49	9.09	8.44	0.37	0.08	0.58	5.74	3.99	0.02	0.01	1.16	99.75	0.45	0.676 (0.013)	0.47
IAMB-S1 <sup>e</sup>	48.14	1.09	8.52	21.31	0.41	9.33	6.45	3.32	0.57	0.86	–	0.00	100.00	0.79	1.000 (0.082)	0.79
IAMB-S3 <sup>e</sup>	53.59	1.03	9.18	16.62	0.34	8.05	5.73	3.85	0.77	0.86	–	0.00	100.00	0.31	0.510 (0.022)	0.28
HDM-S1 <sup>e</sup>	45.23	0.56	10.34	21.04	0.12	11.04	8.27	0.20	2.61	0.60	–	0.00	100.00	0.77	1.000 (0.052)	0.79
HDM-S4 <sup>e</sup>	47.35	0.55	10.75	18.46	0.11	11.04	8.21	0.19	2.73	0.60	–	0.00	100.00	0.20	0.263 (0.010)	0.21
LDM-S1 <sup>e</sup>	42.69	0.68	10.11	21.77	0.15	10.98	8.72	3.60	0.27	1.03	–	0.00	100.00	0.77	1.000 (0.038)	0.79
ETN DRY <sup>d</sup>	48.95	1.67	17.00	10.08	0.24	5.54	10.18	3.72	1.85	0.01	0.47	0.00	99.71	0.76	0.988 (0.024)	0.74
ETN 1.4 <sup>d</sup>	47.96	1.65	16.68	10.17	0.22	5.39	10.09	3.66	1.83	0.02	0.53	1.48	99.68	0.32	0.671 (0.035)	0.35
ETN 2.9 <sup>d</sup>	47.90	1.61	16.62	10.15	0.20	5.29	9.92	3.59	1.78	0.01	0.47	2.40	99.94	0.39	0.845 (0.043)	0.48

<sup>a</sup> From Di Genova et al. (2013).

<sup>b</sup> Raman parameter calculated according to Equation 1.

<sup>c</sup> Calculated Fe<sup>3+</sup>/Fe<sub>tot</sub> ratio using Equation 2.

<sup>d</sup> From Di Genova et al. (2014a).

<sup>e</sup> From Chevrel et al. (2014).



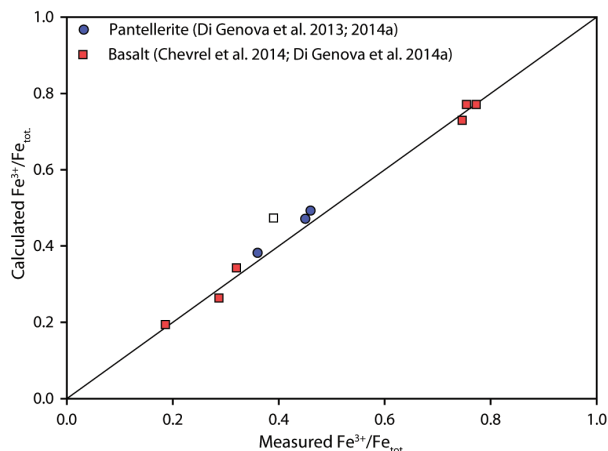


**FIGURE 7.** Comparison between measured  $\text{Fe}^{3+}/\text{Fe}_{\text{tot}}$  ratio using wet chemistry and calculated  $\text{Fe}^{3+}/\text{Fe}_{\text{tot}}$  ratio using our Raman models (Eq. 2) for the samples used to validate the models.  $\text{Fe}^{3+}/\text{Fe}_{\text{tot}}$  ratios and Raman parameters are reported in Table 4. The white square represents the basaltic sample (ETN 2.9) with the highest water content ( $\text{H}_2\text{O}$  2.40 wt%) for which our model shows the highest error in the  $\text{Fe}^{3+}/\text{Fe}_{\text{tot}}$  ratio estimation among the analyzed samples (see Table 4 and text for discussion).

## IMPLICATIONS

Here, we presented an improved Raman spectra database (after Di Genova et al. 2015) including silica-alkali-rich and iron-rich basaltic glasses together with two linear mixing models to estimate the iron oxidation state ( $\text{Fe}^{3+}/\text{Fe}_{\text{tot}}$ ) from the spectra. This study, in addition to the results presented by Di Genova et al. (2015), provides a high spatial resolution ( $\sim 1 \mu\text{m}$ ) tool for detailed studies of the chemical composition and iron oxidation state of glasses. The implications and applications of such a tool are multiple: high spatial resolution tool for estimating chemical composition and iron oxidation state of glasses (from melt inclusions to glass matrix of rocks); in situ and remotely controlled identification, discrimination, and analyses of glasses (determination of chemical composition and iron oxidation state); and planetary science studies (e.g., Mars).

The method presented here is of particular interest for analyses of small quantities of glass such as melt inclusions and glass matrix of crystalline rocks. Indeed, the chemical composition and  $\text{Fe}^{3+}/\text{Fe}_{\text{tot}}$  ratio of melt inclusion is widely used as a chemical indicator of the melt redox conditions during the formation of magmas at depth, both on Earth and other planets. For example, Berry et al. (2008) used XANES to study the iron oxidation state of melt inclusion in komatiite to infer the condition of the Archean mantle.

As documented since the first Apollo missions, amorphous materials, especially iron-rich basaltic, are encountered frequently on the Moon (Shearer et al. 1990). Similarly, several recent studies (Horgan and Bell 2012; Blake et al. 2013; Vaniman et al. 2013; Bish et al. 2014; Downs and MSL Science Team 2015; Grotzinger et al. 2015; Kah and MSL Science Team 2015; Newsom et al. 2015) observed high abundances of alkali-silica-rich amorphous materials in sediment on Mars and martian meteorites.

Herd et al. (2001, 2002) investigated the oxygen fugacity of martian basaltic meteorites. Both studies claim that the oxygen fugacity of the samples varies by 2 log units suggesting that water may play a significant role in the oxidation of basaltic magmas on Mars or, alternatively, a secondary assimilation of ferric-iron-rich material. Our method would allow similar analyses in a much faster and cheaper way than XANES spectroscopy and, importantly, directly in situ and remotely controlled.

The potential of this methodology has recently been demonstrated by Raman apparatus, which were used to perform analyses under extreme conditions (Tarcea et al. 2008; Di Genova et al. 2015 and reference therein). Moreover, both the European Space Agency (ESA) and National Aeronautics and Space Administration (NASA) have established two forthcoming Mars mission [ExoMars program (2016–2018) and Mars 2020], using rovers equipped with Raman spectrometers, to investigate the martian environment to provide information about the potential generation of life and igneous processes on the planet. In this context, in Figure 1 we report a compilation of the chemical analyses recently performed on Mars. Inspection of the diagram reveals that the chemical compositions of the samples used in this work well match the in situ estimated chemical compositions on Mars and, for this reason, we believe that our tool will enhance the interpretive capabilities of the forthcoming Mars missions.

Another applications of our results are the possibility to discriminate the impact vs. volcanic origin of glasses. Indeed, Lukanin and Kadik (2007) presented a review of the available data on the  $\text{Fe}^{3+}/\text{Fe}_{\text{tot}}$  ratio of tektites and impact glasses, concluding that these glasses are more reduced compared with the precursor target material probably related to the characteristics of oxygen, and temperature, regime during the decompression stage following shock compression.

For all these reasons, our study extends the potential use of Raman spectroscopy to a powerful tool able to shed new light on the formation of impact craters and the type of magmatism and volcanic activity in our Solar System.

## ACKNOWLEDGMENTS

This research was funded by the European Union's Seventh Programme for research technological development and demonstration by the ERC Advanced Grant 247076-EVOKES. We thank Daniel R. Neuville and Dominique de Ligny for constructive comments to the manuscript and Dirk Müller for EMP analyses. The authors are grateful to F. Rinaldi, M.R. Cicconi, and S. Kolzenburg for useful discussions and advice. The first author thanks T.W. Duke for the illuminating discussion and inspiring comments that greatly improved the quality of this manuscript.

## REFERENCES CITED

- Baratoux, D., Toplis, M.J., Monnereau, M., and Gasnault, O. (2011) Thermal history of Mars inferred from orbital geochemistry of volcanic provinces. *Nature*, 472, 338–341.
- Behrens, H., and Zhang, Y. (2009)  $\text{H}_2\text{O}$  diffusion in peralkaline to peraluminous rhyolitic melts. *Contributions to Mineralogy and Petrology*, 157, 765–780.
- Bell, R.J., and Dean, P. (1972) The structure of vitreous silica: Validity of the random network theory. *Philosophical Magazine*, 25, 1381–1398.
- Bell, R.J., Bird, N.F., and Dean, P. (1968) The vibrational spectra of vitreous silica, germania and beryllium fluoride. *Journal of Physics C: Solid State Physics*, 1, 299.
- Berry, A.J., O'Neill, H.St.C., Jayasuriya, K.D., Campbell, S., and Foran, G.J. (2003) XANES calibrations for the oxidation state of iron in a silicate glass. *American Mineralogist*, 88, 967–977.
- Berry, A.J., Danyushevsky, L.V., O'Neill, H.St.C., Newville, M., and Sutton, S.R. (2008) Oxidation state of iron in komatiitic melt inclusions indicates hot Archean mantle. *Nature*, 455, 960–963.
- Bish, D.L., Blake, D.F., Vaniman, D.T., Chipera, S.J., Morris, R.V., Ming, D.W., Treiman, A.H., Sarrazin, P., Morrison, S.M., Downs, R.T., and others. (2014)

- X-ray diffraction results from Mars. *Science*, 341, 1238932, 6 p.
- Blake, D.F., Morris, R.V., Kocurek, G., Morrison, S.M., Downs, R.T., Bish, D., Ming, D.W., Edgett, K.S., Rubin, D., Goetz, W., and others. (2013) Curiosity at Gale crater, Mars: characterization and analysis of the Rocknest sand shadow. *Science*, 341, 1239505.
- Borisov, A., Behrens, H., and Holtz, F. (2015) Effects of melt composition on  $\text{Fe}^{3+}/\text{Fe}^{2+}$  in silicate melts: a step to model ferric/ferrous ratio in multicomponent systems. *Contributions to Mineralogy and Petrology*, 169, 23–24.
- Botcharnikov, R.E., Koepke, J., Holtz, F., McCammon, C.A., and Wilke, M. (2005) The effect of water activity on the oxidation and structural state of Fe in a ferro-basaltic melt. *Geochimica et Cosmochimica Acta*, 69, 5071–5085.
- Campany, M., Kamenetsky, V.S., Melgarejo, J.C., Mangas, J., Manuel, J., Alfonso, P., Kamenetsky, M.B., Bambi, A.C.J.M., and Gonçalves, A.O. (2015) Carbonatitic lavas in Catanda (Kwana Sul, Angola): Mineralogical and geochemical constraints on the parental melt. *Lithos*, 232, 1–11.
- Chevrel, M.O., Giordano, D., Potuzak, M., Courtial, P., and Dingwell, D.B. (2013) Physical properties of  $\text{CaAl}_2\text{Si}_2\text{O}_7\text{-CaMgSi}_2\text{O}_7\text{-FeO-Fe}_2\text{O}_3$  melts: Analogues for extra-terrestrial basalt. *Chemical Geology*, 346, 93–105.
- Chevrel, M.O., Baratoux, D., Hess, K.U., and Dingwell, D.B. (2014) Viscous flow behavior of tholeiitic and alkaline Fe-rich martian basalts. *Geochimica et Cosmochimica Acta*, 124, 348–365.
- Cicconi, M.R., Giuli, G., Ertel-Ingrisch, W., Paris, E., and Dingwell, D.B. (2015) The effect of the  $[\text{Na}/(\text{Na}+\text{K})]$  ratio on Fe speciation in phonolitic glasses. *American Mineralogist*, 100, 1610–1619.
- Cukierman, M., and Uhlmann, D.R. (1974) Effects of iron oxidation state on viscosity, Lunar Composition 15555. *Journal of Geophysical Research*, 79, 1594–1598.
- Di Genova, D., Romano, C., Hess, K.U., Vona, A., Poe, B.T., Giordano, D., Dingwell, D.B., and Behrens, H. (2013) The rheology of peralkaline rhyolites from Pantelleria Island. *Journal of Volcanology and Geothermal Research*, 249, 201–216.
- Di Genova, D., Romano, C., Giordano, D., and Alletti, M. (2014a) Heat capacity, configurational heat capacity and fragility of hydrous magmas. *Geochimica et Cosmochimica Acta*, 142, 314–333.
- Di Genova, D., Romano, C., Alletti, M., Misi, V., and Scarlato, P. (2014b) The effect of  $\text{CO}_2$  and  $\text{H}_2\text{O}$  on Etna and Fondo Riccio (Phlegrean Fields) liquid viscosity, glass transition temperature and heat capacity. *Chemical Geology*, 377, 72–86.
- Di Genova, D., Morgavi, D., Hess, K.U., Neuville, D.R., Borovkov, N., Perugini, D., and Dingwell, D.B. (2015) Approximate chemical analysis of volcanic glasses using Raman spectroscopy. *Journal of Raman Spectroscopy*, 46, 1235–1244.
- Di Muro, A., Métrich, N., Mercier, M., Giordano, D., Massare, D., and Montagnac, G. (2009) Micro-Raman determination of iron redox state in dry natural glasses: Application to peralkaline rhyolites and basalts. *Chemical Geology*, 259, 78–88.
- Dingwell, D.B. (1991) Redox viscometry of some Fe-bearing silicate melts. *American Mineralogist*, 76, 1560–1562.
- (2006) Transport properties of magmas: Diffusion and rheology. *Elements*, 2, 281–286.
- Dingwell, D.B., and Virgo, D. (1987) The effect of oxidation state on the viscosity of melts in the system  $\text{Na}_2\text{O-FeO-Fe}_2\text{O}_3\text{-SiO}_2$ . *Geochimica et Cosmochimica Acta*, 51, 195–205.
- (1988) Viscosities of melts in the  $\text{Na}_2\text{O-FeO-Fe}_2\text{O}_3\text{-SiO}_2$  system and factors controlling relative viscosities of fully polymerized silicate melts. *Geochimica et Cosmochimica Acta*, 52, 395–403.
- Dingwell, D.B., Brearley, M., and Dickinson, E. Jr. (1988) Melt densities in the  $\text{Na}_2\text{O-FeO-Fe}_2\text{O}_3\text{-SiO}_2$  system and the partial molar volume of tetrahedrally-coordinated ferric iron in silicate melts. *Geochimica et Cosmochimica Acta*, 52, 2467–2475.
- Dingwell, D.B., Romano, C., and Hess, K.U. (1996) The effect of water on the viscosity of a haplogranitic melt under P-T-X conditions relevant to silicic volcanism. *Contributions to Mineralogy and Petrology*, 124, 19–28.
- Downs, R.T., and MSL Science Team. (2015) Determining mineralogy on Mars with the CheMin X-ray diffractometer. *Elements*, 11, 45–50.
- Furukawa, T., Fox, K.E., and White, W.B. (1981) Raman spectroscopic investigation of the structure of silicate glasses. III. Raman intensities and structural units in sodium silicate glasses. *The Journal of Chemical Physics*, 75, 3226.
- Giuli, G., Paris, E., Pratesi, G., Koerber, C., and Cipriani, C. (2003) Iron oxidation state in the Fe-rich layer and silica matrix of Libyan Desert Glass: A high-resolution XANES study. *Meteoritics and Planetary Science*, 38, 1181–1186.
- Giuli, G., Paris, E., Hess, K.U., Dingwell, D.B., Cicconi, M.R., Eeckhout, S.G., Fehr, K.T., and Valenti, P. (2011) XAS determination of the Fe local environment and oxidation state in phonolite glasses. *American Mineralogist*, 96, 631–636.
- Giuli, G., Alonso-Mori, R., Cicconi, M.R., Paris, E., Glatzel, P., Eeckhout, S.G., and Scaillet, B. (2012) Effect of alkalis on the Fe oxidation state and local environment in peralkaline rhyolitic glasses. *American Mineralogist*, 97, 468–475.
- Grotzinger, J.P., Crisp, J.A., Vasavada, A.R., and MSL Team. (2015) Curiosity's mission of exploration at Gale Crater, Mars. *Elements*, 11, 19–26.
- Herd, C.D.K., Papike, J.J., and Brearley, A.J. (2001) Oxygen fugacity of martian basalts from electron microprobe oxygen and TEM-EELS analyses of Fe-Ti oxides. *American Mineralogist*, 86, 1015–1024.
- Herd, C.D.K., Borg, L.E., Jones, J.H., and Papike, J.J. (2002) Oxygen fugacity and geochemical variations in the martian basalts: Implications for martian basalt petrogenesis and the oxidation state of the upper mantle of Mars. *Geochimica et Cosmochimica Acta*, 66, 2025–2036.
- Hess, K.U., and Dingwell, D.B. (1996) Viscosities of hydrous leucogranitic melts: A non-Arrhenian model. *American Mineralogist*, 81, 1297–1300.
- Horgan, B., and Bell, J.F. (2012) Widespread weathered glass on the surface of Mars. *Geology*, 40, 391.
- Jackson, W.E., de Leon, J.M., Brown, G.E. Jr., Waychunas, G.A., Conradson, S.D., and Combes, J.M. (1993) High-temperature XAS study of  $\text{Fe}_2\text{SiO}_4$  liquid: Reduced coordination of ferrous iron. *Science*, 262, 229–233.
- Kah, L.C., and the MSL Science Team. (2015) Images from Curiosity: A new look at Mars. *Elements*, 11, 27–32.
- Knipping, J.L., Behrens, H., Wilke, M., Göttlicher, J., and Stabile, P. (2015) Effect of oxygen fugacity on the coordination and oxidation state of iron in alkali bearing silicate melts. *Chemical Geology*, 411, 143–154.
- Kress, V.C., and Carmichael, I.S.E. (1991) The compressibility of silicate liquids containing  $\text{Fe}_2\text{O}_3$  and the effect of composition, temperature, oxygen fugacity and pressure on their redox states. *Contributions to Mineralogy and Petrology*, 108, 82–92.
- Lange, R.A., and Carmichael, I.S.E. (1987) Densities of  $\text{Na}_2\text{O-K}_2\text{O-CaO-MgO-FeO-Fe}_2\text{O}_3\text{-Al}_2\text{O}_3\text{-TiO}_2\text{-SiO}_2$  liquids; new measurements and derived partial molar properties. *Geochimica et Cosmochimica Acta*, 2931–2946.
- (1990) Thermodynamic properties of silicate liquids with emphasis on density, thermal expansion and compressibility. *Reviews in Mineralogy and Geochemistry*, 24, 25–64.
- Lee, S.K., and Stebbins, J.F. (2003) Nature of cation mixing and ordering in Na-Ca silicate glasses and melts. *The Journal of Physical Chemistry B*, 107, 3141–3148.
- Long, D.A. (1977) Raman Spectroscopy, pp. 276. McGraw-Hill, Maidenhead, U.K.
- Lukanin, O.A., and Kadik, A.A. (2007) Decompression mechanism of ferric iron reduction in tektite melts during their formation in the impact process. *Geochemistry International*, 45, 857–881.
- Magnier, V., Neuville, D.R., Cormier, L., Roux, J., Hazemann, J.-L., de Ligny, D., Pascarelli, S., Vickridge, I., Pinet, O., and Richet, P. (2008) Kinetics and mechanisms of iron redox reactions in silicate melts: The effects of temperature and alkali cations. *Geochimica et Cosmochimica Acta*, 72, 2157–2168.
- Malfait, W.J., and Sanchez-Valle, C. (2012) Effect of water and network connectivity on glass elasticity and melt fragility. *Chemical Geology*, 346, 72–80.
- McCammon, C.A., Chaskar, V., and Richards, G.G. (1991) A technique for spatially resolved Mössbauer spectroscopy applied to quenched metallurgical slags. *Measurement Science and Technology*, 657–662.
- McMillan, P.F. (1984) A Raman spectroscopic study of glasses in the system  $\text{CaO-MgO-SiO}_2$ . *American Mineralogist*, 69, 645–659.
- McMillan, P.F., and Piriou, B. (1982) The structures and vibrational spectra of crystals and glasses in the silica-alumina system. *Journal of Non-Crystalline Solids*, 53, 279–298.
- Ming, D.W., Gellert, R., Morris, R.V., Arvidson, R.E., Brückner, J., Clark, B.C., Cohen, B.A., D'Uston, C., Economou, T., Fleischer, I., and others. (2008) Geochemical properties of rocks and soils in Gusev Crater, Mars: Results of the alpha particle X-ray spectrometer from Cumberland Ridge to home plate. *Journal of Geophysical Research E: Planets*, 113, E12S39.
- Moretti, R. (2005) Polymerisation, basicity, oxidation state and their role in ionic modelling of silicate melts. *Annals of Geophysics*, 48, 583–608.
- Mysen, B.O. (1991) Relations between structure, redox equilibria of iron, and properties of magmatic liquids. In L. Perchuk and I. Kushiro, Eds., *Physical Chemistry of Magmas SE*, 2 vol. 9, pp. 41–98. Springer, Berlin.
- (1997) Aluminosilicate melts: Structure, composition and temperature. *Contributions to Mineralogy and Petrology*, 127, 104–118.
- (2003) Physics and chemistry of silicate glasses and melts. *European Journal of Mineralogy*, 15, 781–802.
- Mysen, B.O., and Richet, P. (2005) *Silicate Glasses and Melts*, 544 p. Elsevier, Amsterdam.
- Mysen, B.O., and Toplis, M.J. (2007) Structural behavior of  $\text{Al}^{3+}$  in peralkaline, metaluminous, and peraluminous silicate melts and glasses at ambient pressure. *American Mineralogist*, 92, 933–946.
- Mysen, B.O., Virgo, D., and Scanfer, C.M. (1980) Relations between the anionic structure and viscosity of silicate melts—A Raman spectroscopic study. *American Mineralogist*, 65, 690–710.
- Mysen, B.O., Virgo, D., and Seifert, A. (1982) Implications for chemical and physical properties of natural magma. *Reviews of Geophysics and Space Physics*, 20, 353–383.
- Mysen, B.O., Virgo, D., and Seifert, F. (1984) Redox equilibria of iron in alkaline earth silicate melts: relationships between melt structure, oxygen fugacity, temperature and properties of iron-bearing silicate liquids. *American Mineralogist*, 69, 834–847.
- Neuville, D.R. (2006) Viscosity, structure and mixing in (Ca, Na) silicate melts. *Chemical Geology*, 229, 28–41.
- Neuville, D.R., and Mysen, B.O. (1996) Role of aluminium in the silicate network: In situ, high-temperature of glasses and melts on the join  $\text{SiO}_2\text{-NaAlO}_2$ . *Geochimica et Cosmochimica Acta*, 60, 1727–1737.
- Neuville, D.R., Courtial, P., Dingwell, D.B., and Richet, P. (1993) Thermodynamic

- and rheological properties of rhyolite and andesite melts. *Contributions to Mineralogy and Petrology*, 113, 572–581.
- Neuville, D.R., de Ligny, D., and Henderson, G.S. (2014) Advances in Raman spectroscopy applied to earth and material sciences. *Reviews in Mineralogy*, 78, 509–541.
- Newsom, H.E., Mangold, N., Kah, L.C., Williams, J.M., Arvidson, R.E., Stein, N., Ollila, A.M., Bridges, J.C., Schwenzner, S.P., King, P.L., and others. (2015) Gale crater and impact processes—Curiosity’s first 364 Sols on Mars. *Icarus*, 249, 108–128.
- Otonello, G., Moretti, R., Marini, L., and Vetuschi Zuccolini, M. (2001) Oxidation state of iron in silicate glasses and melts: A thermochemical model. *Chemical Geology*, 174, 157–179.
- Papale, P. (1999) Modeling of the solubility of a two-component  $\text{H}_2\text{O}+\text{CO}_2$  fluid in silicate liquids. *American Mineralogist*, 84, 477–492.
- Pasquarello, A., Samthein, J., and Car, R. (1998) Dynamic structure factor of vitreous silica from first principles: Comparison to neutron-inelastic-scattering experiments. *Physical Review B*, 57, 14133–14140.
- Persikov, Y.S., Zharikov, V.A., Bukhtiyarov, P.G., and Pol’skoy, S.F. (1990) The effect of volatiles on the properties of magmatic melts. *European Journal of Mineralogy*, 2, 621–642.
- Pouchou, J.-L., and Pichoir, F. (1991) Quantitative analysis of homogeneous or stratified microvolumes applying the model “PAP”. In K.F.J. Heinrich and D. Newbury, Eds., *Electron Probe Quantitation SE*, 4, pp. 31–75. Springer, Berlin.
- Richet, P. (1984) Viscosity and configurational entropy of silicate melts. *Geochimica et Cosmochimica Acta*, 48, 471–483.
- Robert, G., Whittington, A.G., Stechern, A., and Behrens, H. (2014) Heat capacity of hydrous basaltic glasses and liquids. *Journal of Non-Crystalline Solids*, 390, 19–30.
- Romano, C., Poe, B.T., Mincione, V., Hess, K.U., and Dingwell, D.B. (2001) The viscosities of dry and hydrous  $\text{XAlSi}_3\text{O}_8$  (X = Li, Na, K, Ca-0.5, Mg-0.5) melts. *Chemical Geology*, 174, 115–132.
- Rossano, S., and Mysen, B. O. (2012) Raman spectroscopy of silicate glasses and melts in geological systems. *EMU Notes in Mineralogy*, 12, xvii + 504 pp., Chapter 9.
- Rossano, S., Behrens, H., and Wilke, M. (2008) Advanced analyses of  $^{57}\text{Fe}$  Mössbauer data of aluminosilicate glasses. *Physics and Chemistry of Minerals*, 35, 77–93.
- Sautter, V., Toplis, M.J., Wiens, R.C., Cousin, A., Fabre, C., Gasnault, O., Maurice, S., Forni, O., Lasue, J., Ollila, A., and others. (2015) In situ evidence for continental crust on early Mars. *Nature Geoscience*, 8, 4–11.
- Sehlke, A., Whittington, A., Robert, B., Harris, A., Gurioli, L., and Médard, E. (2014) Pahoehoe to ‘a’ a transition of Hawaiian lavas: an experimental study. *Bulletin of Volcanology*, 76, 879 (20 p.).
- Seifert, F., Mysen, B.O., and Virgo, D. (1982) Three-dimensional network structure of quenched melts (glass) in the systems  $\text{SiO}_2\text{-NaAlO}_2$ ,  $\text{SiO}_2\text{-CaAl}_2\text{O}_4$ , and  $\text{SiO}_2\text{-MgAl}_2\text{O}_4$ . *American Mineralogist*, 67, 696–717.
- Shearer, C.K., Papike, J.J., Simon, S.B., Shimizu, N., Yurimoto, H., and Sueno, S. (1990) Ion microprobe studies of trace elements in Apollo 14 volcanic glass beads: Comparisons to Apollo 14 mare basalts and petrogenesis of picritic magmas. *Geochimica et Cosmochimica Acta*, 54, 851–867.
- Shuker, R., and Cammon, W. (1970) Raman-scattering selection-rule breaking and the density of states in amorphous materials. *Physical Review Letters*, 25, 222–225.
- Stebbins, J.F. (2008) Temperature effects on the network structure of oxide melts and their consequences for configurational heat capacity. *Chemical Geology*, 256, 80–91.
- Stolper, E.M. (1982) Water in silicate glasses: An infrared spectroscopic study. *Contributions to Mineralogy and Petrology*, 81, 1–17.
- Stolper, E.M., Baker, M.B., Newcombe, M.E., Schmidt, M.E., Treiman, A.H., Cousin, A., Dyar, M.D., Fisk, M.R., Gellert, R., King, P.L., and others. (2013) The petrochemistry of Jake\_M: a martian mugearite. *Science*, 341, 1239463.
- Tarcea, N., Frosch, T., Rösch, P., Hilchenbach, M., Stuffer, T., Hofer, S., Thiele, H., Hochleitner, R., and Popp, J. (2008) Raman spectroscopy—A powerful tool for in situ planetary science. *Space Science Reviews*, 135, 281–292.
- Toplis, M.J., and Carroll, M.R. (1995) An experimental study of the influence of oxygen fugacity on Fe-Ti oxide stability, phase relations, and mineral-melt equilibria in ferro-basaltic systems. *Journal of Petrology*, 36, 1137–1170.
- Toplis, M.J., Dingwell, D.B., and Libourel, G. (1994) The effect of phosphorus on the iron redox ratio, viscosity, and density of an evolved ferro-basalt. *Contributions to Mineralogy and Petrology*, 117, 293–304.
- Umari, P., Gonze, X., and Pasquarello, A. (2003) Concentration of small ring structures in vitreous silica from a first-principles analysis of the Raman spectrum. *Physical Review Letters*, 90, 027401.
- Vaniman, D.T., Bish, D.L., Ming, D.W., Bristow, T.F., Morris, R.V., Blake, D.F., Chipera, S.J., Morrison, S.M., Treiman, A.H., Rampe, E.B., and others. (2013) Mineralogy of a mudstone at Yellowknife Bay, Gale Crater, Mars. *Science*, 343, 1243480.
- Whittington, A., Richet, P., Linard, Y., and Holtz, F. (2001) The viscosity of hydrous phonolites and trachytes. *Chemical Geology*, 174, 209–223.
- Wilke, M., Farges, F., Petit, P.E., Brown, G.E., and Martin, F. (2001) Oxidation state and coordination of Fe in minerals: An FeK-XANES spectroscopic study. *American Mineralogist*, 86, 714–730.
- Wilke, M., Schmidt, C., Farges, F., Malavergne, V., Gautron, L., Simionovici, A., Hahn, M., and Petit, P.E. (2006) Structural environment of iron in hydrous aluminosilicate glass and melt—evidence from X-ray absorption spectroscopy. *Chemical Geology*, 229, 144–161.
- Xue, X. (2009) Water speciation in hydrous silicate and aluminosilicate glasses: Direct evidence from  $^{29}\text{Si}\text{-}^1\text{H}$  and  $^{27}\text{Al}\text{-}^1\text{H}$  double-resonance NMR. *American Mineralogist*, 94, 395–398.

MANUSCRIPT RECEIVED AUGUST 18, 2015

MANUSCRIPT ACCEPTED NOVEMBER 14, 2015

MANUSCRIPT HANDLED BY DANIEL NEUVILLE